Structural insights into sodium/iodide symporter (NIS) substrate binding and specificity

Silvia Ravera[1], Juan Pablo Nicola[2], Glicella Salazar de Simone[3], Fred J. Sigworth[4], Erkan Karakas[1], L. Mario Amzel[5#], Mario A. Bianchet[6], and Nancy Carrasco[1&*]

[1]Department of Molecular Physiology and Biophysics, Vanderbilt University, Nashville, TN 37232, USA, [2]Department of Clinical Biochemistry, National University of Córdoba, Córdoba, Argentina, [3]Department of Obstetrics and Gynecology, Columbia University Medical Center, New York, NY 10032, USA, [4]Department of Cellular and Molecular Physiology, Yale School of Medicine, New Haven, CT 06510, USA, [5]Department of Biophysics and Biophysical Chemistry, Johns Hopkins University School of Medicine, Baltimore, MD 21205, USA, and [6]Department of Neurology, Johns Hopkins University School of Medicine, Baltimore, MD 21205, USA.

[#] L.M.A. passed away on August 28, 2021.

[*]Correspondence and requests for materials should be addressed to N.C. (email: nancy.carrasco@vanderbilt.edu)

Abstract

The sodium/iodide symporter (NIS) is the essential plasma membrane protein that mediates active iodide (I^-) transport into the thyroid gland, the first step in the biosynthesis of the thyroid hormones—the master regulators of intermediary metabolism. NIS couples the inward translocation of I^- against its electrochemical gradient to the inward transport of Na^+ down its electrochemical gradient. For nearly 50 years before its molecular identification, NIS was already the molecule at the center of the single most effective internal radiation cancer therapy ever devised: radioiodide ($^{131}I^-$) treatment for thyroid cancer. Mutations in NIS cause congenital hypothyroidism, which must be treated immediately after birth to prevent stunted growth and cognitive deficiency. To date, the structure of NIS has been unknown. Here, we report three structures of rat NIS, determined by single-particle cryo-electron microscopy (cryo-EM): one with no substrates bound, one with 2 Na^+ and 1 I^- bound, and one with 1 Na^+ and the oxyanion perrhenate bound. Structural analyses, functional characterization, and computational studies reveal the substrate binding sites and residues key for transport activity. Our results yield insights into how NIS selects, couples, and translocates anions—thereby establishing a framework for understanding NIS function—and into how it transports different substrates with different stoichiometries and releases substrates from its substrate-binding cavity into the cytosol.

Introduction

Iodide (I^-) is a micronutrient that is key for human health because its oxidized form, iodine, is an essential constituent of the thyroid hormones (THs). In humans, an adequate supply of I^- at the very beginning of life is crucial for preventing I^- deficiency disorders (IDDs), because the THs are critical for embryonic and postembryonic development, particularly that of the central nervous system, lungs, and musculoskeletal system. In addition, the THs are master regulators of cellular metabolism in virtually all tissues at all stages of life[1]. The first step in the biosynthesis of the THs is the active transport of I^- into the thyroid, which is mediated by the product of the SLC5A5 gene: the sodium/iodide symporter (NIS), an intrinsic plasma membrane protein located at the basolateral surface of the thyroid follicular cells. NIS couples the inward translocation of I^- against its electrochemical gradient to the inward transport of Na^+ down its electrochemical gradient[2]. Significant mechanistic insights have been gained by determining how NIS

mutations found in patients with IDDs affect the protein's folding, plasma membrane targeting, and activity[3,4].

Beyond its physiological importance, NIS is also the molecule at the center of the remarkably successful treatment for thyroid cancer based on $^{131}I^-$. Thyroid cancer patients are often treated with $^{131}I^-$ after thyroidectomy: this therapy targets and kills remnant malignant cells that actively accumulate the radioisotope via NIS. Because $^{131}I^-$ treatment of thyroid cancer is so effective and has only relatively minor side effects, there is great interest[3] in expressing NIS exogenously in cancers that do not express it endogenously to render them susceptible to destruction by $^{131}I^-$[5]. In addition, NIS is functionally expressed endogenously not only in several extrathyroidal tissues—such as the salivary glands, stomach, intestine, and lactating breast—but also in primary and metastatic breast cancers[6]. This last finding has opened up the possibility that NIS-mediated $^{131}I^-$ treatment may be as effective against breast cancer as it has been against thyroid cancer for 75 years.

NIS translocates several substrates other than I^-, including oxyanions such as the environmental pollutant perchlorate (ClO_4^-), as well as the imaging substrates pertechnetate ($^{99m}TcO_4^-$) and perrhenate ($^{186}ReO_4^-$, $^{188}ReO_4^-$), which are used in single-photon emission computed tomography (SPECT). For their part, the NIS substrates tetrafluoroborate ($^{18}F\text{-}BF_4^-$) and $^{124}I^-$ are used in positron emission tomography (PET). Indeed, because NIS accumulates its substrates in the cell, it offers higher detection sensitivity than proteins that only bind their ligands stoichiometrically. As a result, NIS is becoming the counterpart of green fluorescent protein (GFP) or luciferase for imaging studies in humans[3,5,7,8]. Although the physiology, biochemistry, biophysics, and cell biology of NIS have all been investigated extensively[1,3], our understanding of its symport mechanism has, until now, been hindered by a lack of high-resolution structures of NIS. Here, we use single-particle cryo-electron microscopy (cryo-EM), molecular dynamics (MD) simulations, and functional studies to gain a structural understanding of how NIS binds its anion substrates with such high affinity, how it translocates anions, and how mutations in NIS lead to congenital IDDs.

Results

Structure determination

Rat NIS shares 89% sequence identity with human NIS (Supplementary Fig. 1) and has similar transport properties[4,9-11]. We have previously shown that glycosylation is not required for NIS activity[9,12]. Hence, to carry out structural studies, we engineered a cDNA coding for a recombinant unglycosylated full-length rat NIS molecule: a triple NIS mutant in which all three Asn residues that are glycosylated were replaced with Gln (N225Q/N485Q/N497Q), with an HA (human influenza hemagglutinin) tag at the N-terminus and HIS and SBP (streptavidin-binding protein) tags at the C-terminus (recombinant tagged NIS, rtNIS). We expressed rtNIS in 293F cells, enriched for cells expressing the protein by flow cytometry with an anti-HA antibody, and demonstrated that its activity is indistinguishable from that of WT NIS (Supplementary Fig. 2 a-c). We then solubilized and purified rtNIS in the presence of a high concentration of NaCl (350 mM). The protein that eluted in the peak fraction and electrophoresed as a single polypeptide was used to determine the structure of NIS by single-particle cryo-EM (Supplementary Fig. 2 f-k).

The cryo-EM map (overall resolution 3.46 Å) reveals that NIS in the micelles assumes a dimeric conformation (Fig. 1a, b) with excellent density for all 26 transmembrane segments (TMSs) (Supplementary Fig. 3a) as well as for significant regions of the extramembrane loops and 17 out of 74 residues in the C-terminus. Well-resolved TMSs of different lengths displayed clearly visible α-helical features. As a result, the map enabled us to build a model of the entire protein from residue 9 to residue 561, with the exception of the loops between TMSs 1 and 2 (residues 34-52), TMSs 5 and 6 (residues 183-188), and TMSs 12 and 13 (residues 483-510), whose lack of density may be attributable to the high flexibility of these regions. To further improve the quality of the map, we applied a symmetry expansion to the particles and carried out a local refinement with a mask designed for a single monomer yielding a new map at 3.30 Å resolution (Supplementary Fig. 2h, k Supplementary Table 1).

The NIS dimers embedded in each micelle are in an antiparallel configuration (Fig. 1a, b). As we have demonstrated, when NIS is endogenously expressed, its N-terminus faces the external milieu and its C-terminus the cytosol[9,12-15]. Thus, it is extremely unlikely that the antiparallel NIS dimers in the micelles are physiological. Instead, the antiparallel configuration resulted from the solubilization and purification process (Supplementary Fig. 2d-g). The two oppositely oriented monomers interact through a two-fold axis perpendicular to TMS 5 and TMS 10 and to their local

symmetry counterparts. No salt bridges are observed at the interface, and there are only two symmetrical pairs of polar residues across the local symmetry axis—S396 and T400—but they do not appear to contribute to forming the dimer by means of hydrogen bonds or water-mediated interactions. Only apolar interactions hold the dimer together. Duplicated by the local symmetry, aromatic stacking of W165 between F385 and F392 in the other monomer allows for a specific interaction required to generate identical dimers in different micelles (Supplementary Fig. 3b).

As predicted[11,16], NIS has a LeuT fold with two 5-helix bundle domains (TMSs 2-6 and 7-11) related by an internal pseudo-two-fold symmetry around an axis through the center of the transporter and perpendicular to the membrane plane (Fig. 1c, Supplementary Figs. 2a, 3). This conserved molecular architecture is common to various membrane transporters that have unrelated sequences and belong to different families[17-21]. The alignment between the two repeats has a root mean square deviation (RMSD) of 3.01 Å for 115 Cα atoms aligned. TMSs 2-6 are related to TMSs 7-11 by a 178° rotation parallel to the plane of the membrane. TMSs 2 and 7 have unwound regions (F67-A70 and G261-A263), which likely bind ions and/or participate in the conformational changes that occur during the transport cycle. An analysis of the secondary structure motifs revealed the presence of π-helices at three positions: 101-105, 247-251, and 366-371. Although the protein was purified in the presence of a high concentration of Na^+ (350 mM), we refer to this structure as Apo-NIS, as it does not contain any densities attributable to bound ions.

The electrostatic potential surface shows that the distribution of charges satisfies the positive-inside rule of transmembrane protein topology (Fig. 1f). The protein adopts an inward-facing conformation similar to those observed for the *Vibrio cholerae* Na^+/galactose transporter (vSGLT)[22] and the human Na^+/glucose transporter (hSGLT1)[21] (Fig. 1 g-h), and opposite that of the outwardly open hSGLT2[20] (Fig. 1i) (Cα RMSDs = 2.9 Å over 313 residues, 3.3 Å over 378 residues, and 3.75 Å over 363 residues, respectively). Although the positions of the TMSs suggest that the conformation is inwardly open, the opening is narrower than those in vSGLT or hSGLT1.

Iodide and sodium binding sites

One of the most remarkable properties of NIS is that—unlike Cl^- channels and transporters, which transport both Cl^- and I^- (with affinities in the mM range)[23]—NIS discriminates between these two anions in an astonishingly exquisite way that is of great physiological significance: it

transports I^- but not Cl^-, even though the concentration of Cl^- in the extracellular milieu (~100 mM) is over 10^5 times that of I^- (<1 μM). To uncover the molecular basis for this selectivity, we determined the structure of NIS with I^- bound to it at 3.12 Å (Supplementary Fig. 5a, Supplementary Table 1). Even though the NIS-I^- structure is highly similar to that of Apo-NIS (RMSD = 0.4 over 432 residues), we observed three additional non-protein densities in the core of the NIS-I^- map that correspond to the substrates. To assign the correct ion to each position, we plotted the density map in the vicinity of each ion site and generated a sphere with a radius of 5 Å from the density center. Starting at an ion position, the map density (which is proportional to the electrostatic potential) was ascertained along 48 radial lines in uniformly distributed directions. The radial density, given as the mean over all angles, is plotted as a black curve (Fig. 2a). The height and width of the peaks are expected to reflect the size of the ions: the positive central peak tends to reflect the nuclear charge, and the width of the peak corresponds to the spatial extent of the ion's electron density[24]. The undershoot reflects the potential outside the valence electrons and will be more negative for an anion. Thus, we conclude that the largest peak (1.5 arbitrary units AU) corresponds to I^-, and the smaller peaks (1.0 and 1.2 AU) to Na^+ (Fig. 2a). The I^- binding site is delimited by residues Q72, V76, M90, Q94, W255, V293, L413, and F417, and has a positive residual charge that further stabilizes the anion. All these residues are 100% conserved from humans to fish (Supplementary Fig. 1); notably, most of them are hydrophobic (Fig. 2b).

In addition to the density in NIS-I^- ascribed to I^-, two other clear densities were present, which were attributed to Na^+ ions. One of them, which we dubbed Na1 because it is the closer one to the I^- (5.3 Å), interacts with Q72 and S416, and is stabilized by a cation-π interaction with the aromatic ring of F417 (Fig. 2c). The other Na^+, by contrast—which we named Na2 (7.4 Å from I^-)—is coordinated by the side chain oxygen atoms of three residues: S69, Y144, and Q72 (Fig. 2c).

To ascertain the functional relevance of the interactions observed, we engineered several amino-acid substitutions at positions 69, 72, 90, 94, 144, 293, 416, and 417. In all cases, I^- transport at steady state (at 20 μM I^-) was substantially reduced, and no I^- was transported at all when the substituted residues were charged (Fig. 2d). Similar results have been reported with substitutions at some of these positions in human NIS[25]. Here we show that the effect of the replacements were clearly not due to impaired NIS mutant protein expression or trafficking to the cell surface, because all mutants were present at the plasma membrane at levels comparable to those of WT NIS, as determined by flow cytometry with an antibody against the extracellularly facing HA tag (Supplementary Fig. 2a, 6). Increasing the concentration of I^- 10-fold (to 200 μM I^-)

caused I^- accumulation by WT NIS to increase 2- to 3-fold, but had a more pronounced effect on the mutants, whose I^- accumulation increased 3- to 20-fold (Supplementary Fig. 7), suggesting that the mutants had a markedly lower affinity for I^- than the WT. To test this hypothesis, we carried out I^- transport assays at initial rates. Indeed, the K_M values of the mutants for I^- were considerably higher (3–30-fold) than that of WT NIS (20-30 μM) (Fig. 2e, Supplementary Fig. 7). All mutant NIS proteins also had a higher K_M for Na^+ than WT NIS (50 mM) (Supplementary Fig. 7). These data are consistent with the fact that the binding of one of the substrates increases the affinity of NIS for the other[26,27].

Oxyanion binding site

Although NIS discriminates finely between I^- and the other halides, it does translocate substrates other than I^-, including the oxyanions $^{99m}TcO_4^-$, ReO_4^-, and ClO_4^- (an environmental pollutant)[3,6,28-30]. Strikingly, whereas NIS transports I^- electrogenically (with a 2 Na^+ : 1 I^- stoichiometry), it transports oxyanions electroneutrally (with a 1 Na^+ : 1 oxyanion stoichiometry)[11,26,31]. To deepen our understanding of oxyanion transport by NIS, we determined the structure of the protein in complex with ReO_4^- at a resolution of 3.15 Å (Supplementary Fig. 5b, Supplementary Table 1). We observed two densities located at approximately the same position as two of the three densities in the NIS-I^- map. We propose, based on an analysis similar to the one carried out for the NIS-I^- structure (Fig. 2a), that the large density corresponds to ReO_4^-, owing to the size (2 AU) and shape of the peak, and the small one (1 AU) to Na^+ (Fig. 3a).

ReO_4^- forms hydrogen bonds with Q72 (2.5 Å) and Q94 (2.8 Å), and it is in close contact (<3.6 Å) with V76, M90, W255, V293, and F417 (Fig. 3b). Na1 is located in a very similar position to the one it occupies in the NIS-I^- structure, and it interacts with the same residues: Q72, S416, and F417 (Fig. 3b). The distance between Na1 and ReO_4^- is smaller (3.9 Å) than that between I^- and Na1 (5.3 Å) (Fig. 2b). No other density was found that could be attributed to Na2, which is consistent with the 1:1 stoichiometry of NIS-mediated oxyanion transport[6,11,26,28,30-32]. That the amino acids shown to coordinate ReO_4^- play a significant role in oxyanion transport was demonstrated by the effects of the amino acid substitutions on ReO_4^- transport (Fig. 3c, Supplementary Fig. 8 a-d). A detailed analysis of the Q72 mutants showed that NIS with Ala, Cys, Glu, or His at this position does not transport at 3 μM ReO_4^-. However, these mutants do transport a modest amount of ReO_4^- when its concentration is increased 10-fold. In agreement with these

data, the K_M of Q72T and Q72N for ReO_4^- was only twice that of WT NIS, whereas that of Q72H was 10 times that of WT NIS (Supplementary Fig. 8 e-h).

Electrogenic versus electroneutral transport

The NIS-ReO_4^- structure differs from the NIS-I^- structure in that the Q72 side chain is shifted 28° from its position in the latter. This relatively small displacement causes Q72 to interact with ReO_4^- through its amino group and shifts the Q72 carbonyl that in NIS-I^- interacts with Na2 to coordinate Na1 and no longer interact with Na2 (Fig. 3d). The movement of Q72 might explain, at least in part, the absence of Na2 in the NIS-ReO_4^- structure and, as a consequence, the electroneutral stoichiometry of Na^+/ReO_4^- transport.

Differential effects of I^-, ReO_4^-, and the absence of anions on the structure of NIS

An alignment of the three structures reveals a critical difference in the position of F67. In the Apo-NIS structure, F67, which is located at the "bottom" of the substrate-binding pocket, points toward the "top" of the pocket. In contrast, binding of both I^- and ReO_4^- causes the side chain of F67 to rotate ~100° away from the ions (Fig. 4a). In the NIS-ReO_4^- structure, the backbone atoms of F67 also move 2 Å away from the center, thereby causing M68 to rotate ~115° upward from its position in both the Apo-NIS and NIS-I^- structures (Fig. 4a). Given the position of the carbonyl of F67, and because amino acid substitutions at position 67 reduce I^- transport more than ReO_4^- transport (Supplementary Fig. 9), we can speculate that the local rearrangements brought about by the replacements interfere with the coordination of Na2 and, consequently, ReO_4^- transport should be less affected.

Using the Caver-Analyst software[33], we identified a hydrophilic tunnel in the Apo-NIS structure delimited by TMSs 2, 4, 7, and 9. This pathway was not present in the structures of NIS with substrate bound to it, suggesting that the latter are in an occluded conformation but poised to open up into the cytosol. Our analysis revealed that F67 blocks access to the cytosol pathway in both substrate-bound structures (Fig. 4b).

To determine whether and, if so, how the substrate-binding pockets open up into the cytoplasm, we ran atomistic MD simulations with the three structures. Computational analysis of the snapshots collected during the MD simulations with all three structures revealed clusters of tunnels with a minimum radius of 1.2 Å (which would allow a Na^+ ion through) starting at the absolute positions of the anions and connecting the substrate-binding pocket to the cytosol.

We ran a 5 μs MD simulation with the NIS-I^- structure and collected frames every 100 ps. A pathway analysis carried out on ~1000 snapshots sampled every 50 ns showed that the most frequent cluster was made up of ~860 tunnels delimited by some of the residues known to be important for NIS function, as was observed for the tunnel in the Apo-NIS structure. This suggested that the cluster corresponded to a substrate-release pathway (Supplementary Fig. 10b-d). However, because the ions were restrained, they were not released even after an aggregated sampling time of 5 μs.

For the NIS-ReO_4^- structure, we ran four different MD simulations, with the substrates unrestrained, collecting ~12,000 frames every 100 ps. A pathway analysis of ~1200 frames sampled every ns revealed that the most frequent cluster was made up of 885 tunnels delimited by some residues known to be important for NIS function (Supplementary Fig. 11). In two of four simulations, ReO_4^- and Na^+ were released through a similar pathway: Na1 exited the binding pocket by interacting with S66, S353, T354, and D191–residues key for NIS function[34]. Of interest, the first NIS mutation reported in a patient with congenital hypothyroidism due to a mutations in NIS was T354P, which renders the protein inactive[16]. The molecular requirement for I^- transport at position 354 is a residue with a hydroxyl group at the β-carbon, which is also the requirement at position 353. When D191 was replaced with a range of other amino acids, only Ser yielded a functional protein—and it only transported 10% as much I^- as WT NIS[34]. In transiting towards the cytosol, ReO_4^- (Fig. 4c) interacts with F67, Y144, N262, Q265, and S358, as shown in the tunnel analysis (Supplementary Fig. 11b-d).

Discussion

In view of all these results, we propose that the structures we obtained correspond to the ones circled with red dotted lines in Fig. 4d. We have shown—on the basis of state occupancies derived from statistical thermodynamics data[26]—that, at physiological concentrations of Na^+, 79% of NIS molecules have two Na^+ ions bound to them, which increases the affinity of NIS for I^- by a factor of 10 (Fig. 4d, green dotted square). We hypothesize that the ternary complex isomerizes, causing NIS to adopt an occluded conformation that poises it to open up into the cytoplasm and release its substrates (Fig. 4d, panel 4-8), and the unloaded symporter isomerizes to bind ions from the extracellular milieu and begin the next transport cycle. The transport cycle of NIS, then, includes minimally the steps just described.

One of the most striking attributes of NIS is its ability to transport I^-, a very scarce ion, at the submicromolar concentrations at which it is found in the extracellular milieu, as it is difficult to bind a halide ion such as I^- with high affinity. There remains, however, a very intriguing open question: Why is the affinity of NIS for I^- so high? The answer lies in the special properties of I^-. As a $4d^{10}5s^25p^6$ moiety (identical to xenon), I^- is surrounded by a large unreactive electron cloud that endows it with unique properties that have been elucidated in previous computational studies. Sun *et al.* [35] investigated the behavior of Na^+ halides in a system with a water/air interface and found that I^- behaves differently than do the other halides: not only does it show the highest number-density close to the interface, but also its radial distribution ($\rho(r)$) has its maximum several Å closer to the water/air interface than those of the other halides. These observations strongly suggest that, given the opportunity, I^- will interact with a hydrophobic environment. In agreement with this conclusion is our experimental evidence that most of the residues surrounding I^- are hydrophobic, and replacing them with polar residues affects NIS activity (Fig. 2b, d-e, Suppl Fig. 7).

The members of the SLC5 family transport a diverse set of substrates, including carbohydrates (glucose, galactose, myoinositol), organic cations (choline), and monocarboxylates (nicotinate, butyrate, etc.); among all these substrates, I^- is the only halide anion[20,21]. Although all these proteins have (or are predicted to have) the same fold, it will not be surprising if critical differences are found when their structures are determined, given that they transport extremely different substrates. Alignment of the sequences of the members of the SLC5 family (Supplementary Fig. 12) shows that certain residues in NIS are unique. For example, Q72 interacts with all three substrates in the NIS-I^- structure, but the equivalent residue is a His in the sugar transporters and an Ala in the choline transporter. Q72H NIS and Q72A NIS are inactive, highlighting the critical role that Q72 plays in NIS function (Fig. 2d).

That nature conserved the same structural fold across proteins that transport substrates as diverse as neurotransmitters, carbohydrates, monocarboxylates, and a halogen anion may indicate that thousands of years of evolution optimized a way to harness the energy stored in the Na^+ electrochemical gradient to transport hydrophilic substrates against their concentration or electrochemical gradients—across the hydrophobic environment of the plasma membrane. To date, the prevailing expectation about a wide variety of mammalian transporters (SERT[19], NaCT[18], NKCC1[17], SGLT1[21], SGLT2[20], etc.) has been that the location of their Na2 binding site will correspond to that of the well-known canonical Na2 binding site in the LeuT structure. However,

Na^+ has only been observed in the structure of one mammalian transporter: SERT[19,36,37] , a member of the SLC6 family. The structure of NIS with Na^+ ions bound that we are reporting here is the first structure of a member of the SLC5 family in which bound Na^+ ions have been visualized. The Na^+ ions bound to NIS are in the cavity; notably, the canonical hydroxy group–containing residues (S353 and T354), though important for NIS function[16,34], are in the exit pathway, not in the binding pocket. This is not entirely surprising, given how different I^- is from leucine or serotonin. Therefore, it will be of great interest to determine whether Na^+ ions bind to other members of the SLC5 family and other families at the same site as they do in NIS, or at other sites different from the canonical site, as in LeuT.

NIS is of great significance in the basic field of plasma membrane transporters and for translational applications ranging from cancer treatment to imaging studies. In addition, NIS has been increasingly important as a reporter molecule in gene transfer studies and clinical trials, making it possible to monitor the delivery of therapeutic genes or oncolytic viruses[3,5]. There is consequently no question that the determination of the NIS structures reported here will have a profound impact. The structures have not only greatly deepened our understanding of the mechanism of NIS activity and the NIS transport cycle, but also enabled us to confirm predictions about the roles of specific amino acids mutated in patients with ITDs in NIS function and targeting to the plasma membrane [3,4] (Supplementary Fig. 13).

There is great interest in exogenously expressing NIS in cancers that do not express it endogenously so that those cancers become sensitives to radioiodide therapy[3,5]. That would require that patients will have their endogenous thyroidal NIS expression downregulated by the administration of thyroid hormones to prevent damage to their thyroid. Because this strategy effectively renders patients temporarily hyperthyroid, it would be desirable to develop a protocol for downregulating NIS expression in the thyroid without making patients hyperthyroid. The structures reported here have helped us identify residues critical for NIS function, such as F67, and their roles in substrate specificity. As a result, we have determined that the F67Q mutant (Supplementary Fig. 9) would be a candidate to express instead of WT NIS in gene transfer studies. Because F67Q NIS transports ReO_4^- but not I^-, patients could be treated with $^{186}ReO_4^-$ while thyroidal NIS is saturated with non-radioactive I^-, thus protecting the thyroid from the radioactivity without causing hyperthyroidism or any other side effects.

Methods

Cell Culture

COS-7 and 293F cell lines obtained from the American Type Culture Collection were cultured in DMEM media (GIBCO) supplemented with 10% FBS (GIBCO), 10 mM glutamine, and 100 U/mL penicillin/streptomycin (GIBCO). 293F cells in suspension were maintained in Free-Style Media (GIBCO) supplemented with 2% FBS.

Site-Directed Mutagenesis

F67, S69, Q72, M90, Q94, Y144, V293, S416, and F417 NIS-mutants were generated using as a template HA-tagged NIS cloned into pcDNA3.1. A PCR was performed with primers carrying the relevant specific codon using Kod Hot Start DNA polymerase (Novagen). After digestion with DpnI (NEB) to eliminate parental DNA, the PCR product was transformed into XL1 Blue Supercompetent *E.coli*. All constructs were sequenced to verify the specific nucleotide substitutions that had been made.

Flow Cytometry

Paraformaldehyde-fixed cells were incubated with 0.1 µg/mL anti-HA (YPYDVPDYA) antibody (Roche Applied Science) in PBS/BSA (0.2%) followed by 50 nM of PE-conjugated goat anti-rat antibody (Life Technologies). The fluorescence of 50,000 cells per sample was assayed with a FACSCalibur flow cytometer (BD Bio-sciences). Data were analyzed using FlowJo software (Tree Star)[34].

Whole-Cell Iodide Transport

Cells were transiently transfected in 10-cm plates using 4 µg HA-tagged NIS in pcDNA3.1 and Lipofectamine/Plus reagent (Life Technologies) or 25 µg cDNAs and PEI MAX (Polyscience). After 24 hrs, they were split into 24 well/plates, and after 48 hrs they were washed twice with HBSS [140 mM NaCl, 5.4 mM KCl, 1.3 mM $CaCl_2$, 0.4 mM $MgSO_4$, 0.5 mM $MgCl_2$, 0.4 mM Na_2HPO_4, 0.44 mM KH_2PO_4, 5.55 mM glucose, and 10 mM Hepes (pH 7.4)] following a previously published protocol[34]. For steady-state experiments, cells were incubated with HBSS containing 10, 20, 100, or 200 µM KI supplemented with carrier-free ^{125}I at a specific activity of 50 µCi/µmol, at 37°C for 45 min in a CO_2 incubator. For I^--dependent kinetic analysis, cells were incubated in HBSS buffer containing the I^- concentrations indicated (1.2-600 µM) for 2 min. Cells were then

washed with HBSS, lysed with ice-cold ethanol, and the intracellular $^{125}I^-$ was quantitated using a Cobra III Gamma Counter (Perkin Elmer).
Kinetic parameters were determined by Michaelis-Menten linear regression after subtraction of the background recorded in cells transfected with a NIS-free plasmid.

Protein Overexpression and Purification

293F cells were transduced with a lentiviral vector containing a rat NIS cDNA construct with an HA tag at the N-terminus and a His8 tag and a streptavidin-binding protein (IBA GmbH) tag at the C-terminus, and they were enriched for positive cells by flow cytometry via HA tag. Up to 97% of positive cells were then grown in suspension[27].
At a density of 2.5×10^6 cells/ml, 293F cells were collected and resuspended in a buffer containing 75 mM Tris·HCl (pH 8.0), 350 mM NaCl, and protease inhibitor cocktail (Roche), and disrupted using an Emulsiflex C3 homogenizer (Avestin). The cell debris was removed by centrifugation at 10,000 × *g* for 10 min, and the membrane-containing supernatant was collected and subjected to ultra-speed centrifugation at 250,000 × *g* for 3 hrs. Membranes were resuspended in the extraction buffer containing 75 mM Tris·HCl (pH 8.0), 350 mM NaCl, and protease inhibitor cocktail (Roche), and incubated with 0.5% LMNG and 0.5% GDN for 2 hrs at 4°C. NIS was subsequently purified via Strep-Tactin® affinity chromatography and size exclusion chromatography via Superdex 200 increase in the presence of 350 mM NaCl, 75 mM Tris·HCl (pH 8.0), and 0.005% LMNG/GDN.
The fraction corresponding to the peak of the chromatogram was then used for EM preparation.

Cryo-Sample Preparation.

All cryo-EM grids were prepared by applying 2.5 µl of protein at ~2 mg/ml to freshly glow-discharged Quantifoil 1.2/1.3, 200 mesh (Electron Microscopy Sciences), blotted for 4-6 s at 100% humidity and 7°C, and plunge-frozen in liquid nitrogen–cooled liquid ethane using a Vitrobot Mark IV (ThermoFisher Scientific).

Data Acquisition and Processing

All the cryo-EM datasets were collected using a Titan Krios G2 electron microscope (Yale University Cryo-EM Resource) operated at 300 kV and equipped with a GIF Quantum LS imaging filter (Gatan, Inc.) and a K3 summit direct electron detector (Gatan, Inc.). Images were acquired at a superresolution pixel size of 0.534 Å. The dose rate was 16.1 e/physical pixel/s, yielding a total dose of 45 e/Å^2. Movie stacks were drift-corrected using MotionCorr2[38] with a 5 × 5 patch

and twofold binning. Contrast transfer function (CTF) information was estimated from dose-weighted images by CTFFind4.1[39].

Two datasets for NIS in the presence of its substrate Na^+ were acquired in two separate sessions from two different protein preparations, yielding 3861 and 4164 movies respectively. Each dataset was analyzed individually. Movie stacks were drift-corrected using MotionCorr2[38] with a 5 × 5 patch and a twofold binning. Contrast transfer function (CTF) information was estimated from dose-weighted images by CTFFind4.1[39] in Relion[40] with exhaustive searching. Particles were picked by Relion Auto-picking using Laplacian-of-Gaussian blob detection. After particles were extracted at a pixel size of 2.73 Å/px, 3 rounds of 2D classification were performed using the fast subset for a larger dataset followed by one with all data. After the good classes were selected, the contributing particles were re-extracted at the original size (1.068 Å/px), and multiple rounds of 3D classification and 3D auto-refinement were performed in Relion. The final particles leading to the best 3D-refined maps in both datasets were combined and subjected to additional 3D classification and 3D Refinement. The final pool of 108k selected particles was extracted with different particle-box sizes and imported in cryoSPARC[41]. Non-Uniform Refinement[42] of the several particle sets led to the choice of the optimal particle-box size (288 px)[43]; subsequent Global CTF Refinement and Non-Uniform Refinement resulted in a 3.47 Å map. The NIS model was built in Coot[44] and refined in Phenix[45] Real Space Refine. Local Resolution analysis was performed in cryoSPARC. We used Chimera[46] to generate a mask around one of the monomers and cryoSPARC to locally refine the map, thereby obtaining a final 3.29 Å map. The model was then further refined in Phenix, yielding the final structure.

A dataset for NIS in the presence of both its substrates Na^+ and I^- (purification buffer supplemented with 2 mM KI) was acquired for a total of 3867 movies. Particles were chosen by Relion Auto-picking using Laplacian-of-Gaussian blob detection, for a total of 3×10^6 particles followed by 3 rounds of 2D classification using the fast subset for a larger dataset and then one last one with all data. After class selection, the particles were re-extracted at the original size (1.068 Å/px), and multiple rounds of 3D classification and 3D auto-refine were performed in Relion 3.0.8. The final pool of particles was then re-extracted with a different box size and imported in cryoSPARC[41]. Non-Uniform Refinement[42] of the several particle sets led to the choice of the optimal particle-box size (288 px)[43]; subsequent Global CTF Refinement and Non-Uniform Refinement resulted in a 3.46 Å map. The NIS model was built in Coot[44] and refined in Phenix[45] Real Space Refine. Local Resolution analysis was performed in cryoSPARC using Local

Resolution Estimation, and the density maps were prepared using UCSF Chimera[46]. We used Chimera to generate a mask around one of the monomers and cryoSPARC to locally refine the map, thereby obtaining a final 3.12 Å map. The model was then further refined in Phenix, yielding the final structure.

A dataset for NIS in the presence of both its substrates Na^+ and ReO_4^- (purification buffer supplemented with 1 mM $NaReO_4$) was acquired, for a total of 4431 movies. Particles were chosen by Relion Auto-picking using Laplacian-of-Gaussian blob detection, for a total of 3×10^6 particles, followed by 3 rounds of 2D classification using the fast subset for a larger dataset and then one last one with all data. After class selection, the particles were re-extracted at the original size (1.068 Å/px), with a different box size and imported in cryoSPARC[41]. Several rounds of Heterogeneous Refinement lead to a final 432k particles that were then subjected to Non-Uniform Refinement[42] and subsequent Global CTF Refinement to obtain a 3.24 Å map. The NIS model was built in Coot[44] and refined in Phenix[45] Real Space Refine. Local Resolution analysis was performed in cryoSPARC. Symmetry expansion and local refinement applying a mask covering a single monomer led to a map with 3.15 Å resolution. The NIS model was then refined in Phenix[45] Real Space Refine.

Ion identification

As a cryo-EM density map reflects electrostatic potentials, we sought to quantitate the density in the vicinity of the ion sites. We ascertained the iodide or perrhenate map density along 24 lines (48 equally spaced directions generated using HealPix pixelation[47]) centered on each ion position. Densities along the lines were evaluated by trilinear interpolation on a four-times Fourier-upsampled density map. An overall spherically averaged density (as a function of radial distance from the ion) was also computed from the upsampled map. To aid comparison of numerical values between maps, density values in each map were normalized using the peak density at the α-carbon positions of the residues Q72 and Q94[24,47].

Molecular Dynamics Simulations

Molecular dynamics simulations were carried out using the NIS apo- and holo-structures (2 Na^+/I^- and Na^+ structures) embedded in a pre-equilibrated 1,2-Dioleoyl-sn-glycero-3-phosphocholine (DOPC) bilayer. We obtained the parameters and scripts for the minimization, equilibration, and production in GROMACS using CHARMM-GUI[48]. The composition of each system in the production runs is summarized in Supplemental Information Table SX. All simulations were

carried out with GROMACS, version 2020[49], in conjunction with the CharMM36 force field[50], using a TIP3P water model[51], Berger-derived DOPC lipids[52], and ion parameters by Joung and Cheatham[53]. Van der Waals interactions were cut off at 1 nm, and electrostatics were treated by PME[54] beyond 1 nm. Temperature and pressure were kept at 310.5 K and 1 bar using the V-Rescale thermostat[55] and Parrinello-Rahman barostat[56], respectively. All bonds were restrained using LINCS[57], and an integration time step of 2 fs was used. We energy-minimized (steepest descent) using a double-precision version of GROMACS, and six steps (125, 125, 125, 500, 500, and 500 ns) of position restraint with a gradually lifted harmonic force constant (Fc) with different values for backbone atoms (100000, 2000, 1000, 500, 200, and 50 kJ/mol/nm^2), side-chain atoms (2000, 2000, 1000, 500, 200, 50, and 0 kJ/mol/nm^2), residue dihedrals (1000, 200, 200, 100, and 0 kJ/mol/nm^2), and lipids (1000, 400, 400, 200, 40, and 0 kJ/mol/nm^2).

Acknowledgements

We thank Dr. Hassane Mchaourab and the members of the Carrasco laboratory for critical reading of the manuscript and insightful discussion. This study was supported by National Institutes of Health grants GM R01 114250 (to NC and LMA) and NS021501 (to FJS). We are grateful to Shenping Wu of the Yale CryoEM Resource facility for screening and data collection. This work was conducted in part using the CPU and GPU resources of the Advanced Computing Center for Research and Education (ACCRE) at Vanderbilt University. We used the DORS storage system supported by the U.S. National Institute of Health (NIH) (S10RR031634 to Jarrod Smith).

Author contributions

S.R., N.C. and L.M.A. conceived the project. S.R. expressed and purified the protein, and prepared cryo-grids. S.R. and E.K. processed the cryo-EM data. S.R., E.K., L.M.A., and M.A.B. built and refined the atomic models. F.J.S. implemented the protocol for ion identification. S.R. and M.A.B. carried out MD simulations. S.R., J.P.N., and G.S.S. generated mutant NIS proteins and carried out functional assays. S.R. and N.C. wrote the manuscript with input from all the other authors.

References

1 Portulano, C., Paroder-Belenitsky, M. & Carrasco, N. The Na(+)/I(-) Symporter (NIS): Mechanism and Medical Impact. *Endocrine reviews* **35**, 106-149, doi:10.1210/er.2012-1036 (2014).

2 Dai, G., Levy, O. & Carrasco, N. Cloning and characterization of the thyroid iodide transporter. *Nature* **379**, 458-460 (1996).

3 Ravera, S., Reyna-Neyra, A., Ferrandino, G., Amzel, L. M. & Carrasco, N. The Sodium/Iodide Symporter (NIS): Molecular Physiology and Preclinical and Clinical Applications. *Annu Rev Physiol* **79**, 261-289, doi:10.1146/annurev-physiol-022516-034125 (2017).

4 Reyna-Neyra, A. *et al.* The Iodide Transport Defect-Causing Y348D Mutation in the Na(+)/I(-) Symporter Renders the Protein Intrinsically Inactive and Impairs Its Targeting to the Plasma Membrane. *Thyroid* **31**, 1272-1281, doi:10.1089/thy.2020.0931 (2021).

5 Spitzweg, C. *et al.* The sodium iodide symporter (NIS): novel applications for radionuclide imaging and treatment. *Endocr Relat Cancer* **28**, T193-T213, doi:10.1530/ERC-21-0177 (2021).

6 Tazebay, U. H. *et al.* The mammary gland iodide transporter is expressed during lactation and in breast cancer. *Nat Med* **6**, 871-878, doi:10.1038/78630 (2000).

7 Urnauer, S. *et al.* EGFR-targeted nonviral NIS gene transfer for bioimaging and therapy of disseminated colon cancer metastases. *Oncotarget* **8**, 92195-92208, doi:10.18632/oncotarget.21028 (2017).

8 Miller, A. & Russell, S. J. The use of the NIS reporter gene for optimizing oncolytic virotherapy. *Expert Opin Biol Ther* **16**, 15-32, doi:10.1517/14712598.2016.1100162 (2016).

9 Li, W., Nicola, J. P., Amzel, L. M. & Carrasco, N. Asn441 plays a key role in folding and function of the Na+/I- symporter (NIS). *FASEB journal : official publication of the Federation of American Societies for Experimental Biology*, doi:10.1096/fj.13-229138 (2013).

10 Nicola, J. P. *et al.* Sodium/Iodide Symporter Mutant V270E Causes Stunted Growth but No Cognitive Deficiency. *J Clin Endocrinol Metab* **100**, E1353-1361, doi:10.1210/jc.2015-1824 (2015).

11 Paroder-Belenitsky, M. *et al.* Mechanism of anion selectivity and stoichiometry of the Na+/I- symporter (NIS). *Proc Natl Acad Sci U S A* **108**, 17933-17938, doi:1108278108 [pii] 10.1073/pnas.1108278108 (2011).

12 Levy, O. *et al.* N-linked glycosylation of the thyroid Na+/I- symporter (NIS). Implications for its secondary structure model. *J Biol Chem* **273**, 22657-22663 (1998).

13 Levy, O. *et al.* Characterization of the thyroid Na+/I- symporter with an anti-COOH terminus antibody. *Proc Natl Acad Sci U S A* **94**, 5568-5573 (1997).

14 Nicola, J. P. *et al.* The sodium/iodide symporter mutant V270E causes stunted growth but no cognitive deficiency. *J Clin Endocrinol Metab*, jc20151824, doi:10.1210/jc.2015-1824

(2015).
15 Paroder, V., Nicola, J. P., Ginter, C. S. & Carrasco, N. The Iodide Transport Defect-Causing Mutation R124H: a δ-amino group at position 124 is critical for maturation and trafficking of the Na+/I- symporter (NIS). *J Cell Sci* **126**, 3305-3313, doi:doi: 10.1242/jcs.120246 (2013).
16 De la Vieja, A., Reed, M. D., Ginter, C. S. & Carrasco, N. Amino acid residues in transmembrane segment IX of the Na+/I- symporter play a role in its Na+ dependence and are critical for transport activity. *J Biol Chem* **282**, 25290-25298, doi:10.1074/jbc.M700147200 (2007).
17 Chew, T. A. *et al.* Structure and mechanism of the cation-chloride cotransporter NKCC1. *Nature* **572**, 488-492, doi:10.1038/s41586-019-1438-2 (2019).
18 Sauer, D. B. *et al.* Structure and inhibition mechanism of the human citrate transporter NaCT. *Nature* **591**, 157-161, doi:10.1038/s41586-021-03230-x (2021).
19 Coleman, J. A., Green, E. M. & Gouaux, E. X-ray structures and mechanism of the human serotonin transporter. *Nature* **532**, 334-339, doi:10.1038/nature17629 (2016).
20 Niu, Y. *et al.* Structural basis of inhibition of the human SGLT2-MAP17 glucose transporter. *Nature*, doi:10.1038/s41586-021-04212-9 (2021).
21 Han, L. *et al.* Structure and mechanism of the SGLT family of glucose transporters. *Nature*, doi:10.1038/s41586-021-04211-w (2021).
22 Faham, S. *et al.* The crystal structure of a sodium galactose transporter reveals mechanistic insights into Na+/sugar symport. *Science* **321**, 810-814, doi:1160406 [pii] 10.1126/science.1160406 (2008).
23 Zhang, Z., Liu, F. & Chen, J. Molecular structure of the ATP-bound, phosphorylated human CFTR. *Proc Natl Acad Sci U S A* **115**, 12757-12762, doi:10.1073/pnas.1815287115 (2018).
24 Wang, J., Liu, Z., Frank, J. & Moore, P. B. Identification of ions in experimental electrostatic potential maps. *IUCrJ* **5**, 375-381, doi:10.1107/S2052252518006292 (2018).
25 Zhekova, H. R. *et al.* Mapping of Ion and Substrate Binding Sites in Human Sodium Iodide Symporter (hNIS). *J Chem Inf Model* **60**, 1652-1665, doi:10.1021/acs.jcim.9b01114 (2020).
26 Nicola, J. P., Carrasco, N. & Amzel, L. M. Physiological sodium concentrations enhance the iodide affinity of the Na+/I- symporter. *Nat Commun* **5**, 3948, doi:10.1038/ncomms4948 (2014).
27 Ravera, S., Quick, M., Nicola, J. P., Carrasco, N. & Amzel, L. M. Beyond non-integer Hill coefficients: A novel approach to analyzing binding data, applied to Na+-driven transporters. *J Gen Physiol* **145**, 555-563, doi:10.1085/jgp.201511365 (2015).
28 Dohan, O. *et al.* The Na+/I symporter (NIS) mediates electroneutral active transport of the environmental pollutant perchlorate. *Proc Natl Acad Sci U S A* **104**, 20250-20255, doi:0707207104 10.1073/pnas.0707207104 (2007).
29 Tran, N. *et al.* Thyroid-stimulating hormone increases active transport of perchlorate into

thyroid cells. *Am J Physiol Endocrinol Metab* **294**, E802-806, doi:10.1152/ajpendo.00013.2008 (2008).

30 Zuckier, L. S. *et al.* Kinetics of perrhenate uptake and comparative biodistribution of perrhenate, pertechnetate, and iodide by NaI symporter-expressing tissues in vivo. *J Nucl Med* **45**, 500-507 (2004).

31 Llorente-Esteban, A. *et al.* Allosteric regulation of mammalian Na(+)/I(-) symporter activity by perchlorate. *Nat Struct Mol Biol*, doi:10.1038/s41594-020-0417-5 (2020).

32 Boutagy, N. E. *et al.* Noninvasive In Vivo Quantification of Adeno-Associated Virus Serotype 9-Mediated Expression of the Sodium/Iodide Symporter Under Hindlimb Ischemia and Neuraminidase Desialylation in Skeletal Muscle Using Single-Photon Emission Computed Tomography/Computed Tomography. *Circ Cardiovasc Imaging* **12**, e009063, doi:10.1161/CIRCIMAGING.119.009063 (2019).

33 Pavelka, A. *et al.* CAVER: Algorithms for Analyzing Dynamics of Tunnels in Macromolecules. *IEEE/ACM Trans Comput Biol Bioinform* **13**, 505-517, doi:10.1109/TCBB.2015.2459680 (2016).

34 Ferrandino, G. *et al.* Na+ coordination at the Na2 site of the Na+/I- symporter. *Proc Natl Acad Sci U S A* **113**, E5379-5388, doi:10.1073/pnas.1607231113 (2016).

35 Sun, L. *et al.* Molecular Dynamics Simulations of the Surface Tension and Structure of Salt Solutions and Clusters. *J Phys Chem* **116**, 3198-3204 (2012).

36 Yang, D. & Gouaux, E. Illumination of serotonin transporter mechanism and role of the allosteric site. *Sci Adv* **7**, eabl3857, doi:10.1126/sciadv.abl3857 (2021).

37 Coleman, J. A. & Gouaux, E. Structural basis for recognition of diverse antidepressants by the human serotonin transporter. *Nat Struct Mol Biol* **25**, 170-175, doi:10.1038/s41594-018-0026-8 (2018).

38 Zheng, S. Q. *et al.* MotionCor2: anisotropic correction of beam-induced motion for improved cryo-electron microscopy. *Nat Methods* **14**, 331-332, doi:10.1038/nmeth.4193 (2017).

39 Rohou, A. & Grigorieff, N. CTFFIND4: Fast and accurate defocus estimation from electron micrographs. *J Struct Biol* **192**, 216-221, doi:10.1016/j.jsb.2015.08.008 (2015).

40 Scheres, S. H. RELION: implementation of a Bayesian approach to cryo-EM structure determination. *J Struct Biol* **180**, 519-530, doi:10.1016/j.jsb.2012.09.006 (2012).

41 Punjani, A., Rubinstein, J. L., Fleet, D. J. & Brubaker, M. A. cryoSPARC: algorithms for rapid unsupervised cryo-EM structure determination. *Nat Methods* **14**, 290-296, doi:10.1038/nmeth.4169 (2017).

42 Punjani, A., Zhang, H. & Fleet, D. J. Non-uniform refinement: adaptive regularization improves single-particle cryo-EM reconstruction. *Nat Methods* **17**, 1214-1221, doi:10.1038/s41592-020-00990-8 (2020).

43 Moriya, T. *et al.* Size matters: optimal mask diameter and box size for single-particle cryogenic electron microscopy. *bioRxiv* (2020).

44 Emsley, P. & Cowtan, K. Coot: model-building tools for molecular graphics. *Acta*

Crystallogr D Biol Crystallogr **60**, 2126-2132, doi:10.1107/S0907444904019158 (2004).

45 Adams, P. D. *et al.* PHENIX: a comprehensive Python-based system for macromolecular structure solution. *Acta Crystallogr D Biol Crystallogr* **66**, 213-221, doi:10.1107/S0907444909052925 (2010).

46 Pettersen, E. F. *et al.* UCSF Chimera--a visualization system for exploratory research and analysis. *J Comput Chem* **25**, 1605-1612, doi:10.1002/jcc.20084 (2004).

47 Górski, K. M. *et al.* HEALPix: A Framework for High-Resolution Discretization and Fast Analysis of Data Distributed on the Sphere. *Astrophysical Journal* **622(2)** (2005).

48 Lee, J. *et al.* CHARMM-GUI input generator for NAMD, GROMACS, AMBER, OpenMM, and CHARMM/OpenMM simulations using the CHARMM36 additive force field. *J Chem Theory Comput* **12**, 405-413 (2016).

49 Abraham, M. J. *et al.* GROMACS: High performance molecular simulations through multi-level parallelism from laptops to supercomputers. *SoftwareX* **1-2**, 19-25, doi:https://doi.org/10.1016/j.softx.2015.06.001 (2015).

50 Huang, J. *et al.* CHARMM36m: an improved force field for folded and intrinsically disordered proteins. *Nat Methods* **14**, 71-73, doi:10.1038/nmeth.4067 (2017).

51 Jorgensen, W. L., Chandrasekhar, J., Madura, J. D., Impey, R. W. & Klein, M. L. Comparison of simple potential functions for simulating liquid water. *J Chem Phys* **79**, 926-935, doi:10.1063/1.445869 (1983).

52 Cordomí, A., Caltabiano, G. & Pardo, L. Membrane Protein Simulations Using AMBER Force Field and Berger Lipid Parameters. *J Chem Theory Comput* **8**, 948-958, doi:10.1021/ct200491c (2012).

53 Joung, I. S. & Cheatham, T. E., 3rd. Determination of alkali and halide monovalent ion parameters for use in explicitly solvated biomolecular simulations. *J Phys Chem B* **112**, 9020-9041, doi:10.1021/jp8001614 (2008).

54 Essmann, U. *et al.* A smooth particle mesh Ewald method. *J Chem Phys* **103**, 8577-8593, doi:10.1063/1.470117 (1995).

55 Bussi, G., Donadio, D. & Parrinello, M. Canonical sampling through velocity rescaling. *J Chem Phys* **126**, 014101, doi:10.1063/1.2408420 (2007).

56 Parrinello, M. & Rahman, A. Polymorphic transitions in single crystals: A new molecular dynamics method. *J Appl Phys* **52**, 7182-7190 (1981).

57 Hess, B., Bekker, H., Berendsen, H. J. & Fraaije, J. G. LINCS: a linear constraint solver for molecular simulations. *J Comput Chem* **18**, 1463-1472 (1997).

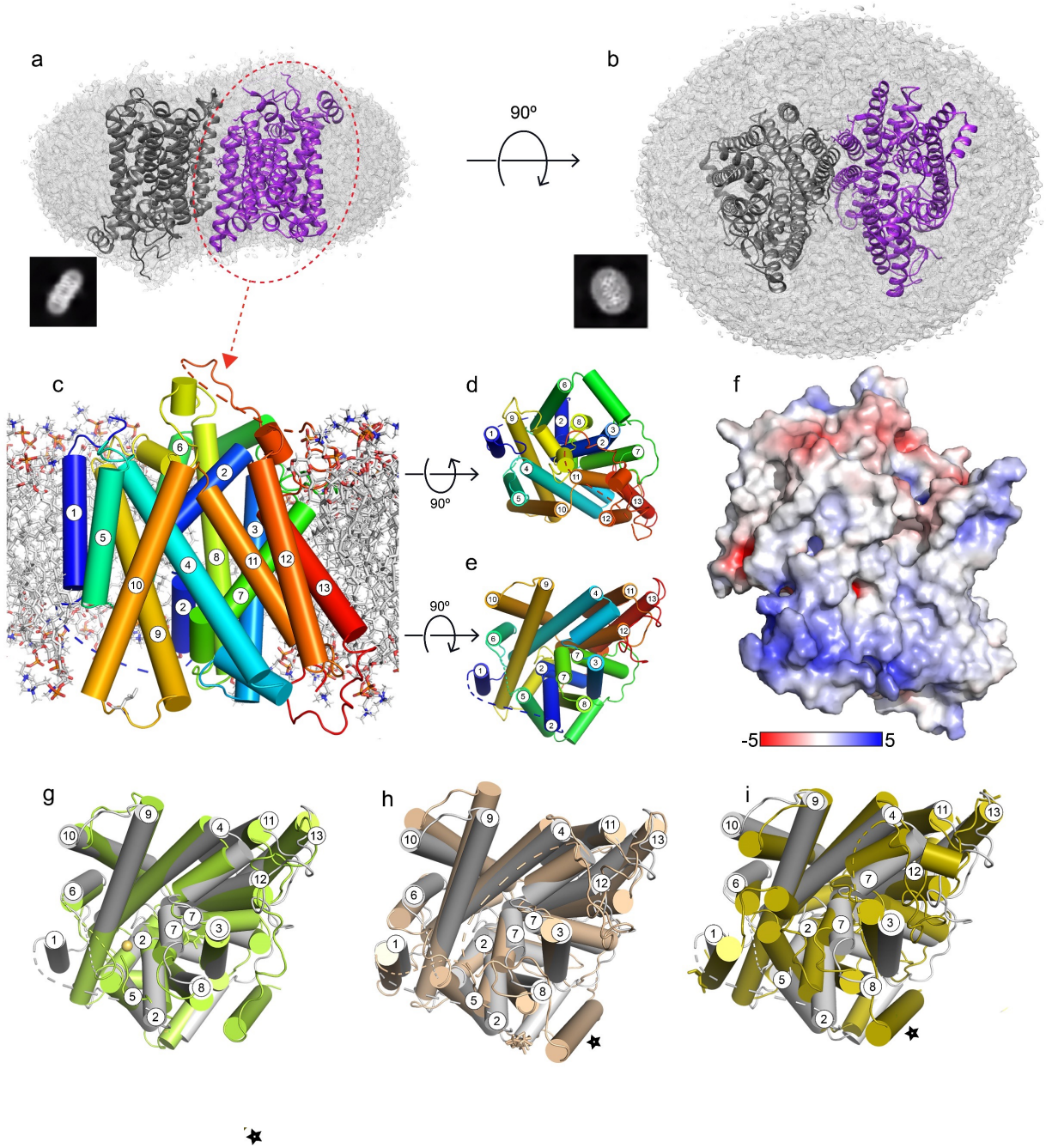

Fig. 1 Structure of NIS. a-b. NIS entirely embedded in a detergent micelle. **a**. Side view. **b.** Top view. Examples of 2D classes representing the corresponding views are shown in the black squares.) **c.** NIS structure viewed from the plane of the membrane, with the numbered TM helices depicted as cylinders; **d**, the corresponding top view, and **e**, bottom view. **f.** Side view of NIS as in (c) but with surface colored according to the electrostatic potential in k_BT/e (red, negative; blue, positive). **g-h**. Structural alignment between NIS in grey, vSGLT in green (g), hSGLT1 in wheat (h), and hSGLT2 in olive (i). * the stars in g, h and i indicate the extra TMS present in vSGLT, SGLT1, and SGLT2.

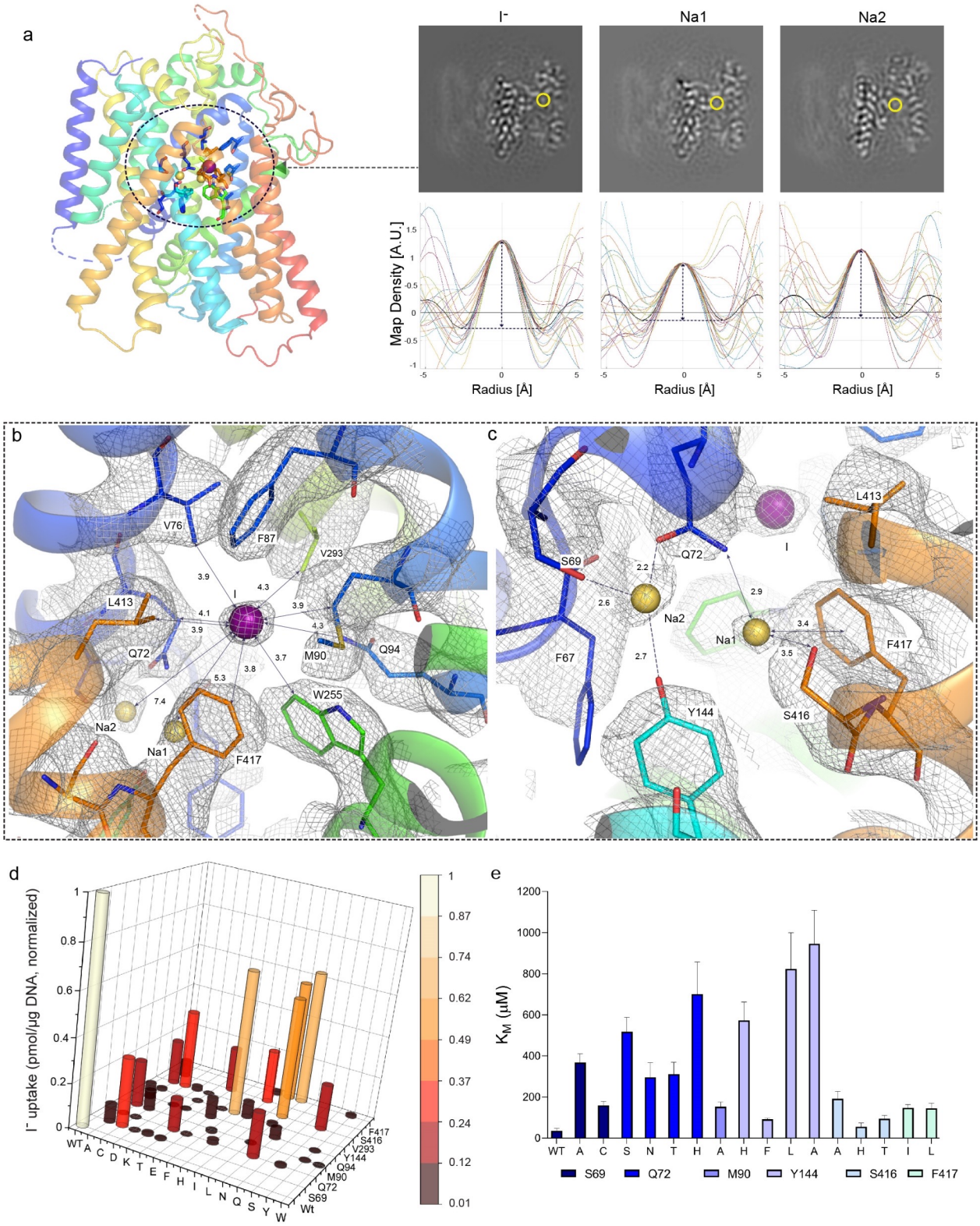

Fig. 2 Iodide binding site in NIS. a. In the Iodide-bound structure, the yellow circle indicates the substrate binding pocket. Ions transported by NIS were identified by analyzing the map density values (map slices in upper panels) along 24 lines passing through each site, circled in yellow. Map values are plotted for each line (lower panels),

and the spherically-averaged mean is plotted in black. **b.** Close-up of the I^- binding pocket, where I^- is represented by the purple sphere. The distance (in Å) from I^- to each surrounding residue is indicated. Yellow spheres represent sodium ions. **c**. Close-up of interactions between Na1 and Na2 and surrounding residues. **d.** Functional effects of mutations in binding-site residues. Steady-state transport was determined at 20 μM I^- and 140 mM Na^+ for 30 min as the difference of rates in the absence or presence of the NIS-specific inhibitor ClO_4^-, normalized to values obtained with WT NIS. **e.** K_M values obtained from the kinetic analysis of I^- transport.

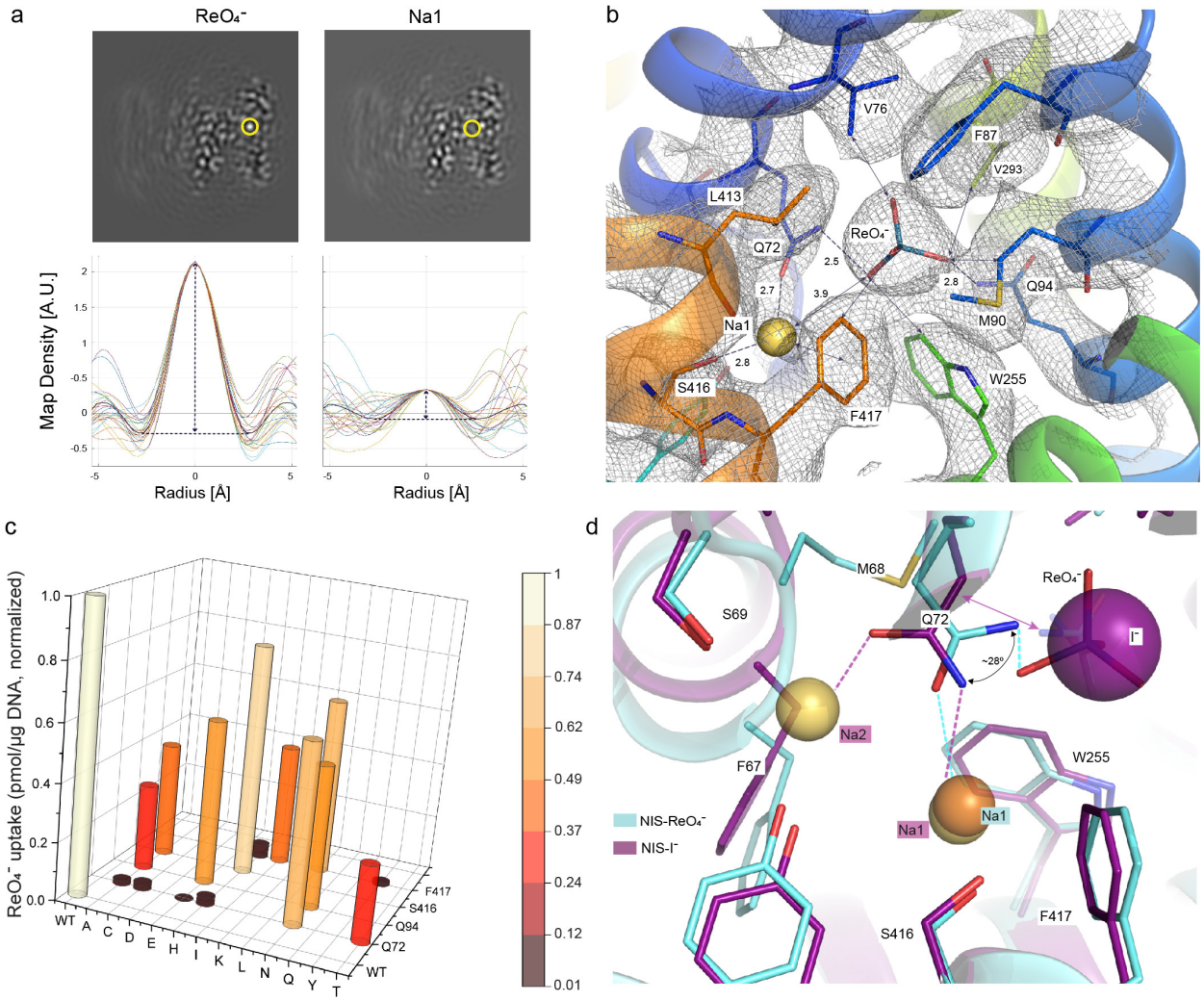

Fig. 3 Perrhenate binding pocket. a. The ions transported by NIS were identified by evaluating the map density along 24 lines passing through each site (circled in yellow on images of map slices). Corresponding values along lines are plotted in colors and the mean as a function of radius in black (bottom panels). **b.** Close-up of the ReO_4^- binding pocket. ReO_4^- is represented by sticks and Na1 by a yellow sphere. Distances from ReO_4^- and Na1 to surrounding residues (within 3.9 Å) are indicated, as is the distance from ReO_4^- to Na1. **c.** Effects of substitutions in binding-site residues, quantified by ReO_4^- transport at steady state (measured at 3 µM ReO_4^- and 140 mM Na^+ for 30 min as the difference in uptake in the absence and presence of the NIS-specific inhibitor ClO_4^-). Values are normalized to those obtained with WT NIS. **d**. Close-up of the structural alignment of NIS-I^- and NIS-ReO_4^- showing the shift of Q72.

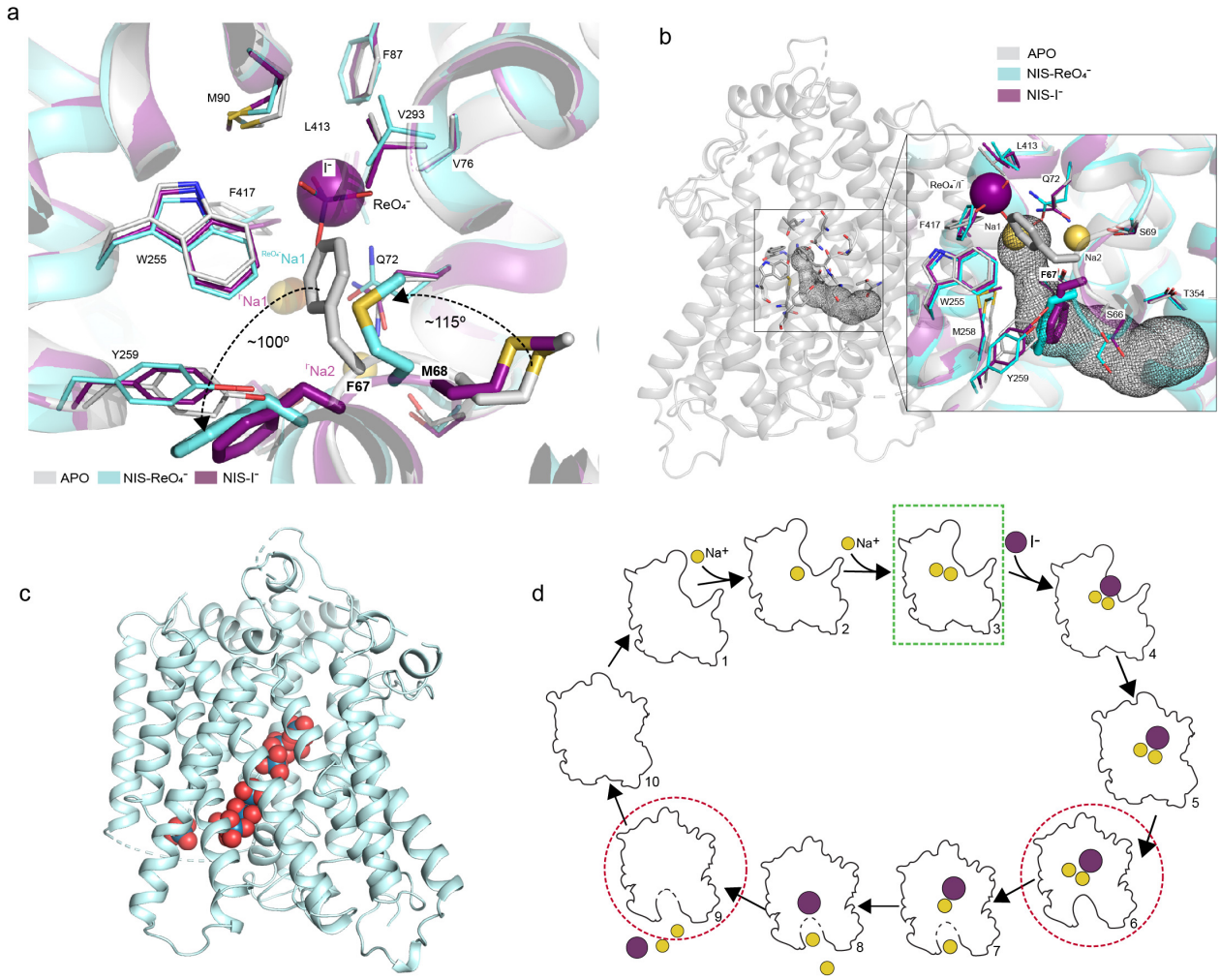

Fig. 4 NIS mechanism. a. Close-up of the structural alignment between Apo-NIS, NIS-I^- and NIS-ReO_4^-. The arrows represent the shift of F67 and M68 from the position they occupy in the Apo-NIS structure to the one in the substrate-bound structures. **b.** Tunnel calculated by Caver-Analyst in the Apo-NIS structure that connects the substrate binding pocket with the cytosol. Inset: alignment of the three structures revealing that in the substrate-bound NIS, F67 blocks the pathway from the binding sites to the cytosol. **c**. Exit pathway of ReO_4^- revealed by the position of the anion in selected frames from the MD simulations. **d.** cartoon representing the putative transport cycle of NIS. The experimental structures are highlighted in red dotted circles and the state hypothesized by statistical thermodynamics, at physiological concentrations of Na^+, is indicated by the green dotted square.